Journal of
Applied Remote Sensing

RemoteSensing.SPIEDigitalLibrary.org

Application of ERS and Envisat cross-interferometry to generation and accuracy assessment of digital elevation model over northern Alaska

Won-Jin Lee
Hyung-Sup Jung
Zhong Lu

SPIE.

Application of ERS and Envisat cross-interferometry to generation and accuracy assessment of digital elevation model over northern Alaska

Won-Jin Lee,[a] Hyung-Sup Jung,[a,*] and Zhong Lu[b]
[a]University of Seoul, Department of Geoinformatics, 90 Jeonnong-dong, Dongdaemun-gu, Seoul 130-743, Republic of Korea
[b]Southern Methodist University, Roy M. Huffington Department of Earth Sciences, Dallas, Texas 75275-0395, United States

Abstract. The accuracy of a digital elevation model (DEM) generated from synthetic aperture radar (SAR) interferometry (InSAR) crucially depends on the length of the perpendicular baseline between SAR acquisitions. ERS-2 and Envisat cross-InSAR (CInSAR) are superior methods to create high precise DEM because the perpendicular baseline can be extended sufficiently long by compensating a slight difference in radar carrier frequency. We have assessed the accuracy of DEM generated by using ERS and Envisat satellite CInSAR techniques using the ice, cloud, and land elevation satellite global elevation data, which has an absolute vertical accuracy of about 2 cm. The study area is high flat land covered up with ice and snow in northern Alaska. Our result shows that the CInSAR-derived DEM can achieve an accuracy of about 0.50 m. This is much better than that of the National Elevation Dataset (DEM) (1.95 m) and is slightly lower than that of the airborne InSAR DEM (0.36 m). [DOI: 10.1117/1.JRS.9.096065]

Keywords: synthetic aperture radar; interferometric synthetic aperture radar; cross-interferometric synthetic aperture radar; digital elevation model; ice, cloud, and land elevation satellite.

Paper 14396 received Jul. 2, 2014; accepted for publication Mar. 16, 2015; published online Apr. 7, 2015.

1 Introduction

Digital elevation models (DEMs) are required for many applications, such as volcanic activity mapping,[1,2] watershed and groundwater monitoring,[3] land subsidence measurement,[4–6] urban studies,[7–9] etc. Various remote sensing data and techniques have been used to construct DEMs, which include stereomapping,[10–12] LIDAR technique,[13,14] and interferometric synthetic aperture radar (InSAR).[15–18] The InSAR method can generate a precise DEM from the InSAR phase that is mainly contributed by the topographic height.[19] It can be also used for the measurements including surface displacements, land topography, land changes, land subsidence/uplift, water levels, soil moisture, snow accumulation, stem volume of forest, etc.[20] Using this technique, the Shuttle Radar Topography Mission was carried out to produce a global DEM for the region between the latitudes of N60° and S56°,[17] and the TanDEM-X mission can meet the challenge of delivering a global DEM with absolute and relative vertical accuracies of 10 and 2 m, respectively.[21,22]

However, the DEM generation based on repeat-pass InSAR imagery has limitations because it largely depends on (1) temporal decorrelation, (2) baseline decorrelation, and (3) atmospheric artifact.[15,17] The temporal decorrelation is caused by surface modifications during the acquisition time interval of the InSAR pair. A long time interval of repeat-pass SAR acquisitions can cause loss of coherence, especially over snow/ice and vegetated terrains. The baseline decorrelation depends on the length of the perpendicular baseline. This may dominate any other decorrelation factors in a rugged terrain. A shorter perpendicular baseline can preserve better coherence in an interferogram, but the vertical accuracy of InSAR-derived DEM is worse due to the larger height

*Address all correspondence to: Hyung-Sup Jung, E-mail: hsjung@uos.ac.kr
1931-3195/2015/$25.00

ambiguity. This trade-off makes it difficult to generate a precise DEM with repeat-pass InSAR images. The atmospheric artifact is caused by the difference of atmospheric delays between two SAR acquisitions and can result in a large-scale DEM error.[17]

If SAR images used for an InSAR pair are simultaneously obtained, the temporal decorrelation and the atmospheric artifact can be fully ignored. Nevertheless, the trade-off between the perpendicular baseline and the coherence cannot be overcome by the conventional InSAR method. Recently, a cross-interferometric synthetic aperture radar (CInSAR) technique based on ERS-2 and Envisat InSAR images has been demonstrated.[23–28] This technique is theoretically capable of generating a submeter-accuracy DEM because it overcomes the trade-off between the perpendicular baseline and the coherence under the condition that the effect of the perpendicular baseline can be exactly compensated by a difference in radar carrier frequency between the two SAR acquisitions. This ERS-2 and Envisat satellite CInSAR technique has the advantages that (1) the temporal decorrelation and the atmospheric artifact can be mostly ignored because the CInSAR pair is acquired with a short repeat-time of about 29 min and (2) the small height ambiguity can be achieved along with high coherence for a CInSAR interferogram with a baseline of ~2 km. A feasibility test and theoretical accuracy have been investigated for a high precise DEM generated using the CInSAR method,[23,25,26] but the accuracy assessment of the CInSAR-derived DEM has not been performed by using precise elevation data which have enough points available to estimate statistical figures.

In this paper, we have conducted a feasibility test about the application of the ERS and Envisat satellite CInSAR technique to precisely generate DEM over high flat land covered up with ice and snow in northern Alaska. Accuracy of the CInSAR-derived DEM has been assessed using the ice, cloud, and land elevation satellite (ICESat) global elevation data, which has an absolute vertical accuracy of about 2 cm.[29] We have, respectively, assessed the accuracy of the CInSAR-derived DEM using the ICESat data of summer and winter seasons to make sure of the snow cover effect. We have used an optimal CInSAR processing procedure to generate the highly precise DEM, which is designed to minimize the phase distortion by the orbit error and to maximize the phase unwrapping efficiency. We have also compared the CInSAR DEM with an airborne InSAR DEM with a spatial resolution of 5 m and vertical error of 1 m over northern Alaska.[30] In addition, we have demonstrated the feasibility of identifying and correcting artifacts in the existing DEM using the CInSAR technique. Our investigations have demonstrated that the CInSAR technique can create DEMs of submeter accuracy over high flat land covered with ice and snow.

2 Methodology

2.1 *Description of Cross-Interferometry*

The SAR system observes the Earth's surface under a specific radar carrier frequency and incidence angle. If the incidence angle or the radar carrier frequency is changed, the range spectrum will be changed.[31] The coherence between two acquisitions can be preserved when the spectra of the two signals are overlapped. The frequency shift of the range spectrum (Δf) can be defined as[31]

$$\Delta f = -\frac{cB_{\perp}}{\lambda\rho\,\tan(\theta-\delta-\alpha)}, \tag{1}$$

where c is the velocity of light, $B_{\perp}$ is the perpendicular baseline, λ is the radar wave length, ρ is the slant range distance, θ is the incidence angle, α is the terrain slope angle, and δ is the inclination angle of the baseline. The frequency is a function of the perpendicular baseline. If the perpendicular baseline is small, the frequency shift is small and then the spectra of the two signals would be overlapped. Otherwise, the frequency shift is large so that the spectra of the two signals would not be overlapped. However, the large frequency shift can be compensated by a frequency difference between two SAR acquisitions, hence the spectra of the two signals can be overlapped. That is, if the difference of the carrier frequencies between ERS-2 and Envisat is very close to the frequency shift calculated from Eq. (1), the spectra of ERS-2 and Envisat can be overlapped. The creation of a coherent ERS-2 and Envisat CInSAR interferogram is based on this principle.

The cross-interferometric phase (φ_{cross}) between master and slave images can be defined as

$$\varphi_{\text{cross}} = \frac{4\pi}{c}(f_2\rho_2 - f_1\rho_1) = \frac{4\pi}{c}(f_1\Delta\rho + \Delta\bar{f}\rho_2), \tag{2}$$

where ρ_1 and ρ_2 are the slant range distances of master and slave images, respectively, f_1 and f_2 are the carrier frequencies of master and slave images, respectively, and $\Delta\rho = \rho_2 - \rho_1$ and $\Delta\bar{f} = f_2 - f_1$. The CInSAR phase can be approximated:[32]

$$\varphi_{\text{cross}} = \frac{4\pi}{c}[-f_1 B\ \sin(\theta - \delta - \alpha) + \Delta\bar{f}\rho_2], \tag{3}$$

where B is the baseline. Hereafter, the inclination angle of the baseline (δ) will not be counted for the sake of simplification because it is small in case of large baseline. By considering the local curvature of the Earth and the terrain slope angle,[31,32] the derivative of the CInSAR phase with respect to the slant range (ρ_2) can be approximated to

$$\frac{\partial\varphi_{\text{cross}}}{\partial\rho_2} = -\frac{4\pi f_1 B_\perp}{c\rho_2\ \tan(\theta - \alpha)} + \frac{4\pi}{c}\Delta\bar{f}. \tag{4}$$

In Eq. (4), the second term on the right side corresponds to the phase gradient due to the difference of the carrier frequencies between master and slave images. Given the system parameters of ERS-2 and Envisat, the phase gradient of the second term is about 1.3 rad/m,[26] and the phase difference in a single range pixel of about 7.8 m reaches about 10.1 rad.

If the fringe rate across the CInSAR interferogram due to Earth's curvature, which is caused by the perpendicular baseline, exceeds 2π rad/range cell, then the InSAR pair will be completely decorrelated. This is called baseline decorrelation and the length at which complete decorrelation occurs is the critical baseline. To avoid this baseline decorrelation, the absolute of the CInSAR phase slant range derivative should be less than

$$\left|\frac{\partial\varphi_{\text{cross}}}{\partial\rho_2}\right| \leq \frac{2\pi}{\Delta_\rho}, \tag{5}$$

where Δ_ρ is the range resolution cell of a single range pixel. Using Eqs. (4) and (5), Fig. 1 shows the change of the phase gradient with respect to the perpendicular baseline and the terrain slope angle for the ERS-2 and Envisat CInSAR. A coherent CInSAR interferogram can be obtained if the perpendicular baseline of the CInSAR pair and the terrain slope angle of the study area fall within the coherent area (see Fig. 1). Otherwise, the CInSAR interferogram is fully decorrelated. The coherent area of the fore slope ($\alpha > 0$) is smaller than that of the back slope ($\alpha < 0$) due to the foreshortening effect of the SAR image. Supposing that the study area consists of flat terrains of less than ± 5 deg, CInSAR pairs of perpendicular baseline between 1.0 and 2.6 km should be selected for the generation of coherent CInSAR interferograms (see Fig. 1).

Topographic effects can also be obtained by a Taylor series expansion of the CInSAR phase in Eq. (3) with respect to the radius of Earth's spheroid (r_e).[32] The derivative of the CInSAR phase with respect to the actual radius of the Earth (r) is approximated to

$$\frac{\partial\varphi_{\text{cross}}}{\partial r}(r_e) = -\frac{4\pi f_1 B_\perp}{c\rho_2\ \sin\theta_e}, \tag{6}$$

where θ_e is the look angle to the Earth spheroid and the derivative of the second term of the right side in Eq. (3) with respect to the actual radius of the Earth is zero because the slant range ρ_2 is considered as a constant. In Eq. (6), $\partial\varphi_{\text{cross}}/\partial r$ can be derived from $(\partial\varphi_{\text{cross}}/\partial\theta)\cdot(\partial\theta/\partial r)$. The total unwrapped phase into topographic height as a function of range is

$$(\varphi_{\text{cross}} - \varphi_e) = -\frac{4\pi f_1 B_\perp}{c\rho_2\ \sin\theta_e}h, \tag{7}$$

where ϕ_e is the phase difference on the Earth spheroid and h is the topographic height defined by $(r - r_e)$. From Eq. (7), the ambiguity height of the CInSAR interferogram (h_a) can be defined as

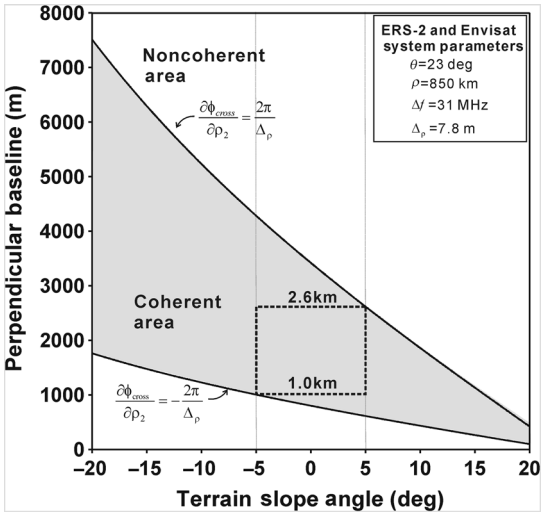

Fig. 1 The change of the flat-Earth phase gradient with respect to the perpendicular baseline and the terrain slope angle in the case of the ERS-2 and Envisat cross-interferometric synthetic aperture radar (CInSAR). The graph has been created by using Eqs. (4) and (5).

$$h_a = \frac{c\rho_2 \sin\theta}{2f_1 B_\perp}. \tag{8}$$

The equation is similar to the conventional InSAR interferogram. Given the system parameters of ERS-2 and Envisat, the ambiguity height is about 4.7 m when the perpendicular baseline is 2000 m. This small height ambiguity enables the generation of high-precision DEM. The measurement uncertainty of the CInSAR-derived height is theoretically calculated from Eq. (7) using mathematical properties of standard deviation as given by

$$\sigma_h = \left| \frac{c\rho_2 \sin\theta_e}{4\pi f_1 B_\perp} \right| \sigma_{\varphi,\text{cross}}, \tag{9}$$

where σ_h and $\sigma_{\varphi,\text{cross}}$ are the standard deviations of the height measurements and the CInSAR phase, respectively.

The standard deviation of the CInSAR phase $\sigma_{\varphi,\text{cross}}$ can be defined using the maximum-likelihood estimator (MLE) as follows:[33]

$$\sigma_{\varphi,\text{cross}} \approx \frac{1}{\sqrt{2N_L}} \frac{\sqrt{1-\gamma^2}}{\gamma}, \tag{10}$$

where N_L is the effective number of looks, γ is the total correlation as[34]

$$\gamma = \frac{|\gamma_{\text{spatial,temporal}}|}{1 + \text{SNR}^{-1}}, \tag{11}$$

where SNR is the system signal-to-noise ratio. The number of looks N_L can be approximately calculated by the number of azimuth and range pixels and reduced by $(1 - \Delta f_{\text{DC}}/B_{\text{D}})$, where Δf_{DC} is the difference of the Doppler centroids between ERS-2 and Envisat acquisitions and B_{D} is the processed Doppler bandwidth. The reduction is attained because the azimuth resolution degrades with the decrease in the processed Doppler bandwidth by the azimuth common band filtering. Similarly, SNR is also reduced by $(1 - \Delta f_{\text{DC}}/B_{\text{D}})$ because the total along-track integration time decreases. A theoretical standard deviation of the CInSAR-derived DEM is shown in Fig. 2. The nominal processing parameters are $\theta = 23$ deg, $\rho = 850.0$ km, $f_1 = 5.3$ GHz, and $N_L = 2.5$. The number of looks N_L is determined by the size of the average widow of 1×5 pixels and $\Delta f_{\text{DC}}/B_{\text{D}} = 0.5$. As shown in Fig. 2, the height uncertainty rapidly increases as the total decorrelation increases. When correlations are 0.9, 0.7, and 0.5 and the perpendicular

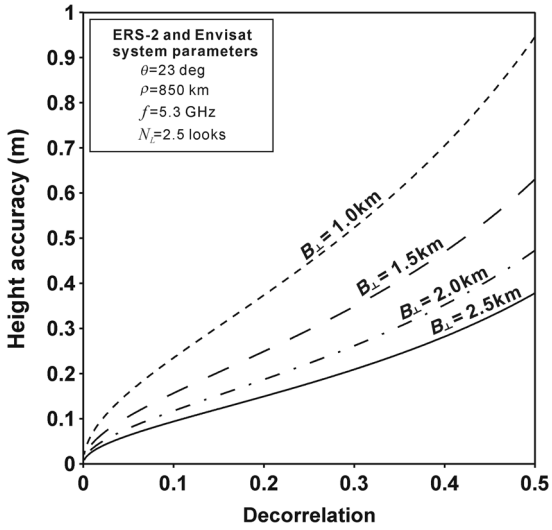

Fig. 2 Theoretical height accuracy of the CInSAR-derived digital elevation model (DEM) with respect to the decorrelation.

baseline is 1000 m, height accuracies are ~24, 52, and 95 cm, respectively, while the height accuracies are about 10, 21, and 38 cm, respectively, when correlations are 0.9, 0.7, and 0.5 and $B_\perp = 2500$ m. Therefore, the performance of the DEM generation using the CInSAR method greatly depends on the correlation and perpendicular baseline of the CInSAR pair. This height accuracy is also degraded by the orbital error and the atmospheric distortions. A perpendicular baseline error of 5 cm, which is the radial orbit precision of ERS,[35] leads to a height error of about 13 cm.[36] In the case of a nonturbulent atmospheric condition, a temporal variation of 30 min can delay the radar signal by about 1 mm.[37] For a baseline of 2500 m, a path delay of 1 mm corresponds to a height error of about 13 cm. Consequently, a CInSAR-derived DEM with submeter height accuracy can be expected.

2.2 *CInSAR-Derived DEM Generation Procedure*

Since the height accuracy of the CInSAR-derived DEM depends on coherence, a key issue in the CInSAR processing is to enhance coherence as much as possible. The detailed CInSAR processing flow used for this study is summarized in Fig. 3. This processing is composed of six steps: (1) generation of single look complex (SLC) images by azimuth common band filtering, (2) coregistration of SLC images at subpixel level determined by searching for local maxima from the two-dimensional cross-correlation surface calculated between oversampled SAR images, (3) generation of differential CInSAR interferogram by the removal of flat-Earth and topographic phases from an existing DEM, (4) unwrapping of differential CInSAR interferogram, (5) refinement of perpendicular baseline using a second order polynomial model, and (6) conversion of the unwrapped CInSAR phases into topographic height.

In this CInSAR processing, a precise coregistration is performed after applying the azimuth common band filtering, but not earlier. The azimuth common band filtering changes the imaging geometry because the Doppler centroids of the CInSAR pair are changed by the filtering. This means that the azimuth shifts in the interferometric pair can result from the azimuth common band filtering. To reduce the shift effect, the azimuth shift is applied before coregistration. For this reason, this step can reduce the phase noise level of the CInSAR interferogram. A CInSAR interferogram is generated by complex conjugate multiplication of the master SLC image with the coregistered slave SLC image and then the range common band filtering is applied to the CInSAR interferogram. A differential CInSAR interferogram is generated by subtracting a synthetic interferogram from the CInSAR interferogram and is then unwrapped. The synthetic interferogram is simulated from an existing DEM and is used to remove the flat-Earth and topographic phase contributions. In order to minimize the flat-Earth and topographic phase distortions by the perpendicular baseline error and to maximize the phase unwrapping efficiency

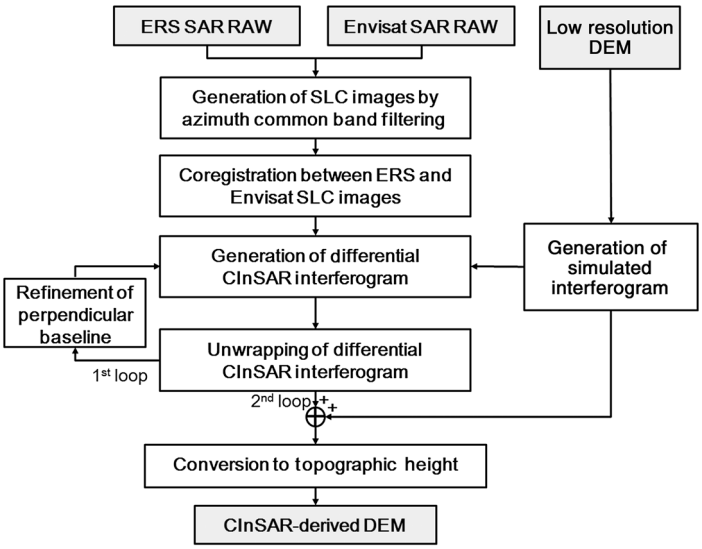

Fig. 3 Block diagram of the optimal CInSAR method used for this study.

through the fringe rate reduction, we have used the differential CInSAR interferogram rather than the CInSAR interferogram for DEM generation. Since the baseline error originates from orbit position accuracy, the unwanted phases generated by the baseline error cannot be removed directly from the orbital parameters. Thus, the perpendicular baseline is refined by a second order polynomial fitting method. The residual phase of the differential CInSAR interferogram (φ_{res}) is fitted into a second order polynomial as given by

$$\varphi_{\text{res}}(t_a, \rho_2) = a_0 + a_1 t_a + a_2 \rho_2 + a_3 t_a \rho_2 + a_4 t_a^2 + a_5 \rho_2^2, \tag{12}$$

where t_a is an azimuth time and $a_0, \ldots,$ and a_5 are the model parameters. The derivative of the residual flat-Earth phase with respect to the slant range (ρ_2) is calculated from the fitted polynomial as

$$\frac{\partial \varphi_{\text{res}}}{\partial \rho_2} = a_2 + a_3 t_a + 2 a_5 \rho_2. \tag{13}$$

Then the residual baseline is calculated from the derivative of the residual flat-Earth phase as given by

$$B_{\perp,\text{res}} = -\frac{c\rho_2 \tan(\theta - \alpha)}{4\pi f_1} \cdot \frac{\partial \varphi_{\text{res}}}{\partial \rho_2}, \tag{14}$$

and the perpendicular baseline is updated by adding the residual baseline.[38] The unwrapped CInSAR interferogram is created by adding the synthetic interferogram back to the differential CInSAR interferogram which is unwrapped using the minimum cost flow algorithm developed by the GAMMA software. Finally, the CInSAR-derived DEM is generated by converting the unwrapped CInSAR phase into the topographic height and correcting the X, Y, and Z offsets of the topographic heights using ground control points (GCP) extracted from ICESat elevation data. The offsets in the X- and Y-directions are calculated from the maximum value of correlation coefficients between the GCP and heights extracted from the CInSAR-derived topographic heights in adjacent positions of the GCP. After determining X and Y offsets, the Z offsets are estimated by a first order polynomial fitting in order to remove the residual orbital error in the CInSAR-derived topographic heights.

The study area is located near Teshekpuk Lake, northern Alaska (see Fig. 4). The area is a high flat land covered with ice and snow and contains many lakes and rivers. The ERS-2 and Envisat data acquired on the descending orbit of January 25, 2008, are used for this study. As shown in Table 1, the ERS-2 and Envisat systems have different carrier frequencies as well as

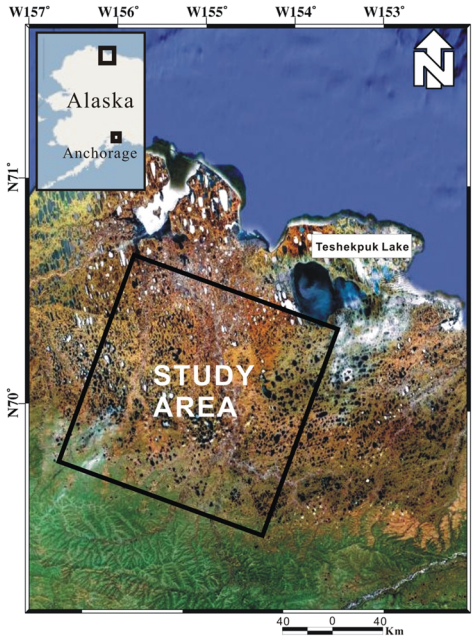

Fig. 4 Study area located near Teshekpuk Lake, northern Alaska.

different sampling and pulse repetition frequencies. The difference in carrier frequency is the reason why the CInSAR technique can allow for the generation of a precise DEM. However, the differences in the sampling frequency and the pulse repetition frequency make the coregistration of ERS-2 and Envisat images more difficult because they, respectively, cause different azimuth and range pixel sizes. The acquisition time difference, Doppler centroid frequency difference, and perpendicular baseline between ERS-2 and Envisat systems are about 29 min, about 405 Hz and about 2321 m, respectively. As aforementioned, we can generate a coherent interferogram from this CInSAR pair because the interferometric coherence can be preserved if the perpendicular baseline of the CInSAR pair is between ~1.0 and 2.6 km in a flat area (see Fig. 1). The system parameters of the ERS-2 and Envisat cross pair used in this study are summarized in Table 1.

The National Elevation Dataset (NED) DEM is used to generate a differential CInSAR interferogram. This NED DEM is a seamless elevation model covering the United States at a resolution of about 30 to 60 m with a vertical accuracy of 2.44 m.[39] NED DEM has been produced from multiple sources by minimizing the artifacts that originate from elevation discrepancies between different sources.[39] An airborne InSAR DEM, which has a spatial resolution of 5.0 m and a vertical accuracy of 1.0 m is compared with CInSAR-derived DEM and NED DEM. The airborne InSAR DEM was generated using the Intermap STAR-3i airborne InSAR system mounted in a LearJet 36A aircraft.[29] The ICESat global elevation data are also used for

Table 1 Comparison of ERS-2 and Envisat system parameters.

System parameters	ERS-2	Envisat
Carrier frequency (GHz)	5.3	5.331
Sampling frequency (MHz)	19.0	19.2
Pulse repetition frequency (Hz)	1679.9	1652.4
Satellite velocity (m/s)	7085.9	7086.2
Mean incidence angle (deg)	23.4	22.8
Azimuth pixel size (m)	3.9	4.0
Slant range pixel size (m)	7.9	7.8

assessing the vertical accuracy of the CInSAR-derived DEM. The ICESat is Earth's first polar-orbiting satellite laser altimeter mission launched in February 2003. The Geoscience Laser Altimeter System (GLAS) sensor mounted on the ICESat provides 15 products in different data processing levels.[40] Among the products, GLA14 is the land surface elevation product. The GLA14 elevation information is estimated by fitting the centroid of the Gaussian distribution within the footprint whose diameter is about 62 m[41] and its absolute vertical accuracy is about 2 cm.[30] We have used the parameters of the acquisition date, latitude, longitude, elevation, and geoid height extracted from the GLA14 product in this study.

3 Results

The DEM generation procedure used for this study has been carried out using the ERS-2 and Envisat CInSAR pair acquired on January 25, 2008 (see Table 2). We first apply the azimuth common band filter to ERS-2 and Envisat raw data to minimize the difference of imaging geometries. The processed Doppler centroid is about −142.5 Hz, which is calculated by averaging the Doppler centroids of ERS-2 and Envisat data, and the processed Doppler bandwidth is about 927.0 Hz, which is called the common band. This overcomes the difficulty in coregistrating the CInSAR pair. The SLC images are obtained by the scaled inverse Fourier transformation designed to preserve phase information. For the subpixel-level coregistration processing, the Envisat image is resampled into the coordinates of the ERS-2 images, the the CInSAR interferogram is generated by the complex conjugate operation of the ERS-2 and the resampled Envisat images, then the range common band filtering is applied to the CInSAR interferogram.

A differential CInSAR interferogram is created by subtracting the synthetic interferogram, which is simulated from the existing NED DEM, from the CInSAR interferogram to correct the flat-Earth and topographic phases. A multilook operation is applied by a two-step strategy such as: (1) 0.5×1 looks in azimuth and range directions before the flat-Earth and topographic phase corrections and (2) 2×5 looks ($\sim$20 m $\times$ 20 m) after the corrections. This strategy might minimize the phase distortion off high fringe rates on CInSAR interferograms, which is caused by a high flat-Earth phase gradient and small height ambiguity. Thus, this strategy can improve the interferometric coherence as much as possible although it requires more processing time and data storage. The differential CInSAR interferogram is unwrapped successfully as the fringe rates are low. To estimate the perpendicular baseline error, the residual flat-Earth phase gradient is calculated from the unwrapped differential CInSAR interferogram by a second-order polynomial fitting method.[37] Consequently, the differential CInSAR interferogram is updated by the refined perpendicular baseline estimated from the residual flat-Earth phase. This update procedure is essential to correct the orbit error.

Figure 5 represents the synthetic interferogram simulated from NED DEM and the unwrapped differential CInSAR interferogram. It is noted that the fringes of Fig. 5 show the scale of 0 to 4π.

The synthetic interferogram in Fig. 5(a) has high fringe rates caused by the small height ambiguity of about 4.1 m. The fringe rates originate from the flat-Earth and topographic phase distortions. Unwrapping this interferogram is difficult due to the high fringe rate. Figure 5(b) represents the differential CInSAR interferogram in which flat-Earth and topographic phases are removed by the synthetic interferogram. The mean of coherences over whole interferogram is about 0.55. The differential CInSAR interferogram shows almost zero phase in most of the study area. However, the nonzero parts of the differential CInSAR interferogram originate from serious errors of NED DEM. Consequently, we can identify the DEM errors in the existing NED

Table 2 Characteristics of cross-interferometric pair used in this study.

Acquisition date	Acquisition time difference (min)	Δf_{DC}[a] (Hz)	$B_{\perp}$[b] (m)
January 25, 2008	29.46	405	2321

[a]Doppler centroid difference.
[b]The perpendicular baseline.

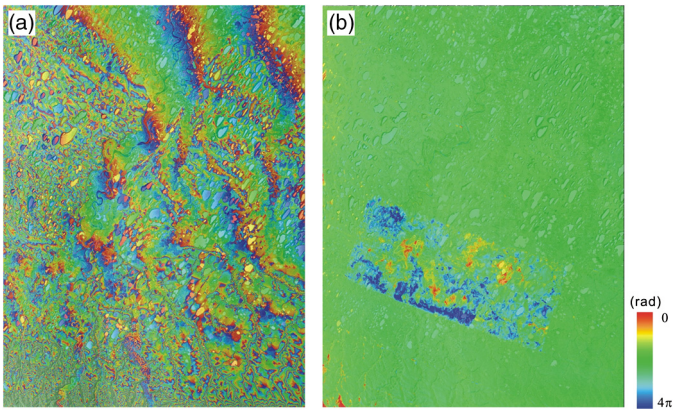

Fig. 5 (a) Synthetic interferogram simulated from National Elevation Dataset (NED) DEM. (b) Unwrapped differential CInSAR interferogram.

DEM from the differential interferogram [see Fig. 5(b)]. This means that the CInSAR technique can be used to find serious errors of the existing DEM.

The differential CInSAR interferogram is smoothed using the adaptive filter with a window size of 64 to reduce interferometric phase noise[42] and is then unwrapped. Then the unwrapped CInSAR interferogram is created by adding back the synthetic interferogram to the unwrapped differential CInSAR interferogram. Finally, we have generated the CInSAR-derived DEM through a phase to height conversion and offset correction. The offset correction was performed by using the ICESat global elevation data from the black dashed lines of Fig. 6, which shows the DEM created by the CInSAR method over northern Alaska. The black dashed lines represent ICESat tracks obtained during February to March 2008, which are close to the SAR data acquisition date. The estimated horizontal offsets were 3.9 and −1.3 m in the X- and Y-directions, respectively, and Z offsets were estimated in the range from −1.5 to 1.5 m.

Figure 7 compares the CInSAR-derived DEM with the NED DEM and the airborne DEM. [Figures 7(a), (d), (g), 7(b), (e), (h)], and 7(g), (h), (i) show the color-coded shade relief maps of the NED, the CInSAR DEM and the airborne DEM in the boxes A, B, and C of Fig. 6, respectively. As seen in Figs. 7(a), (d), (g) and 7(b), (e), (h), the NED DEM does not show the subtle

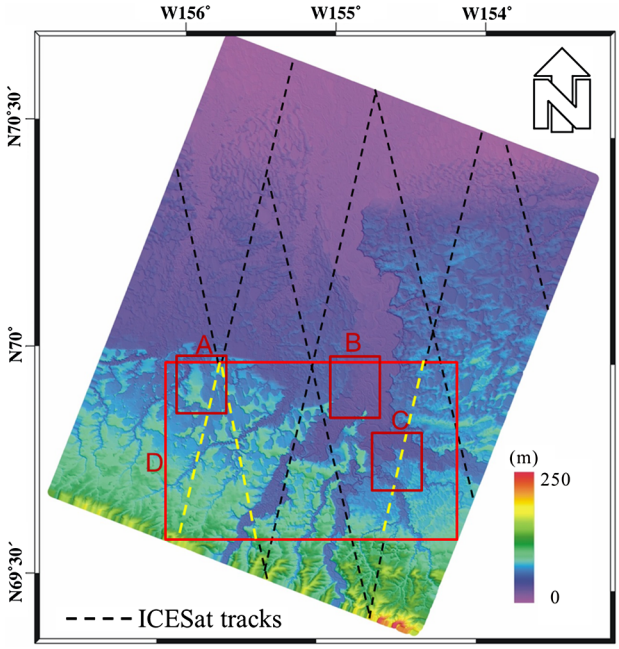

Fig. 6 DEM created by the CInSAR method over study area of Fig. 4.

features of rivers and valleys very well, whereas the CInSAR-derived DEM can distinctly show these features.

Moreover, the NED DEM has artifacts that reach to about 10 m [Figs. 7(d) and 7(g)], while the artifacts are clearly corrected in the CInSAR-derived DEM [Figs. 7(e) and 7(h)]. Although the topographic details of the CInSAR-derived DEM are worse than those of the airborne DEM due to lower resolution, the CInSAR-derived DEM accurately depicts the topographic difference over the study area [Figs. 7(b), 7(e), and 7(h)].

To validate the achieved accuracy of the CInSAR-derived DEM and compare its accuracy with the accuracies of the NED and airborne DEM, we have calculated the accuracies of the three types of DEM using the ICESat global elevation data in the yellow dashed lines of Fig. 6. The accuracy tests were carried out by two different ICESat global elevation datasets in order to make sure of the snow cover effect. One was obtained from the yellow dashed lines during February to March 2008, which is close to the SAR data acquisition date. The limited time may minimize the variation in the snow depth. The other was obtained from the yellow dashed lines in June 2005 and 2006. The study area was not covered by snow during those dates. We cannot find the qualified ICESat elevation data from summer seasons between 2007 and 2009, because there are clouds over the study area in the summer season.

Figure 8 shows the errors of the NED DEM, the CInSAR DEM, and the airborne DEM estimated by the reference to the winter ICESat elevation data of the yellow dashed lines, respectively. The DEM elevations used for the error calculation are extracted by Gaussian average of the elevation values in a grid of 60 m $\times$ 60 m to consider the ICESat footprint diameter of about 62 m. The cell size of the grid is the spatial resolution of the DEM data and the elevation values in the grid are extracted from the DEM by the bicubic interpolation. From this result, the corresponding DEM biases are 0.15, -0.05, and -0.53 m, respectively. The histogram of the DEM difference from the NED DEM is different from those of the CInSAR and airborne DEMs as the NED DEM contains artifacts.

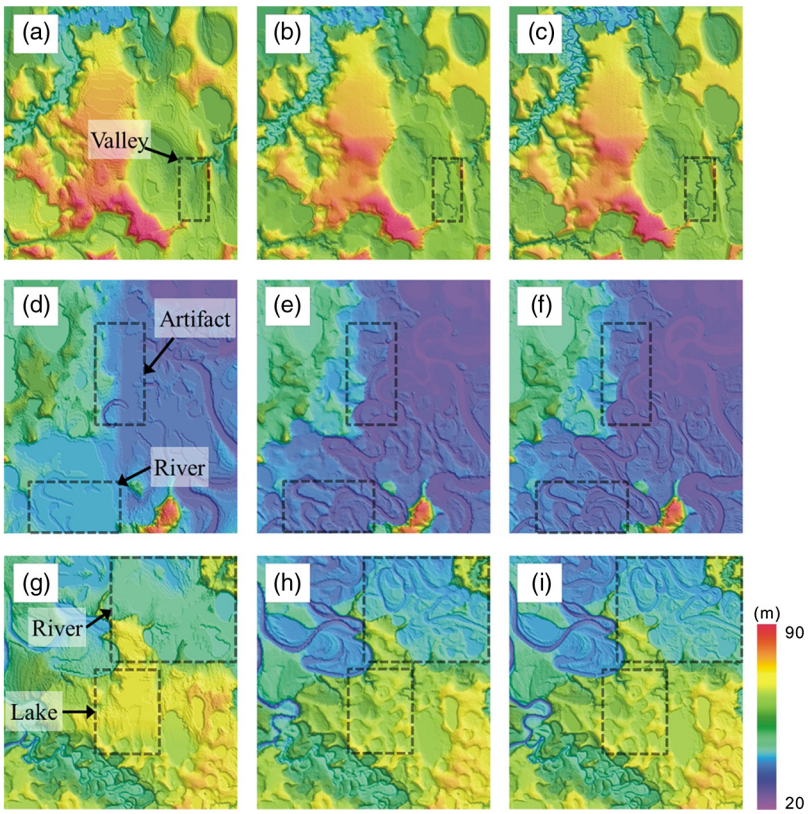

Fig. 7 Comparison among NED, CInSAR-derived, and airborne DEM in the boxes A, B, and C of Fig. 6: (a, d, and g) NED DEM, (b, e, and h) CInSAR-derived DEM, and (c, f, and i) airborne DEM.

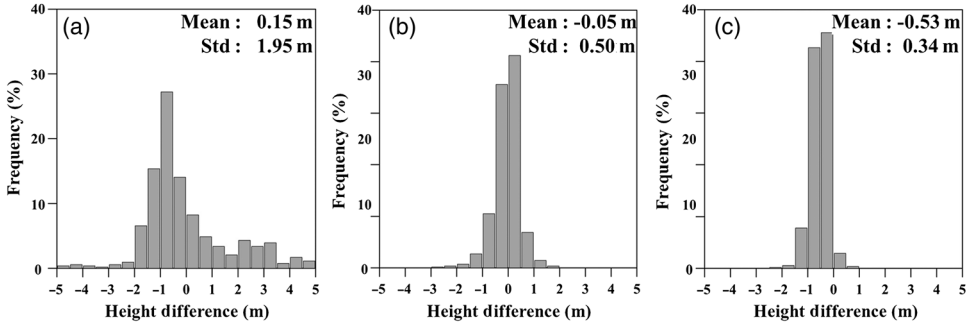

Fig. 8 Error histograms of (a) NED DEM, (b) CInSAR-derived DEM, and (c) airborne DEM. The topographic heights of the winter ice, cloud, and land elevation satellite (ICESat) are used for the reference values.

The bias of the airborne DEM is larger than that of the CInSAR DEM because the airborne DEM was obtained in the summer season. The airborne DEM does not include the snow depth, whereas the winter ICESat elevation data include the snow depth. Thus, the negative bias of the airborne DEM approximately corresponds to the average depth of the snow cover over the study area. The snow depth information was not provided over the study area. However, the snow depth measured in the nearest site at Barrow airport (about 150 km from the study area) was about 35.6 cm in February to March 2008. The bias of the CInSAR DEM is close to zero, because the Z offset of the CInSAR DEM was corrected by using the winter ICESat elevation data. The CInSAR and airborne DEM have a Gaussian distribution while the NED DEM does not (Fig. 8). This means that the NED DEM possesses systematic errors. The standard deviations of the NED DEM, the CInSAR DEM, and the airborne DEM are 1.95, 0.50, and 0.34 m, respectively. Although the accuracy of the CInSAR DEM is 1.5 times lower than that of the airborne DEM, the achieved accuracy of the CInSAR DEM is as precise as it corresponds to approximately a half meter. The theoretical accuracy of the CInSAR DEM with a perpendicular baseline of 2300 m and the coherence of 0.55 is about 0.48 m when the perpendicular baseline error and atmospheric artifact are considered. The atmospheric delay of 1 mm, which occurs in a normal condition, can lead to height error of 13 cm, as previously mentioned in Sec. 2.1. The theoretical accuracy further confirms the achieved accuracy of the CInSAR DEM.

Figure 9 shows the error histograms of the NED DEM, the CInSAR DEM, and the airborne DEM estimated by the reference to the summer ICESat elevation data of the yellow dashed lines, respectively. The corresponding DEM biases are 0.41, 0.45, and 0.02 m, respectively. The bias of the CInSAR DEM approximately corresponds to the average snow depth over the study area because the CInSAR DEM includes the snow depth while the summer ICESat elevation data does not include the snow depth. The bias of the airborne DEM is close to zero because the airborne DEM was produced from airborne InSAR pairs acquired in the summer season. The standard deviations of the NED DEM, the CInSAR DEM, and the airborne DEM are 1.46, 0.56, and 0.36 m, respectively. Although the accuracy of the CInSAR DEM is 1.5 times lower than that of

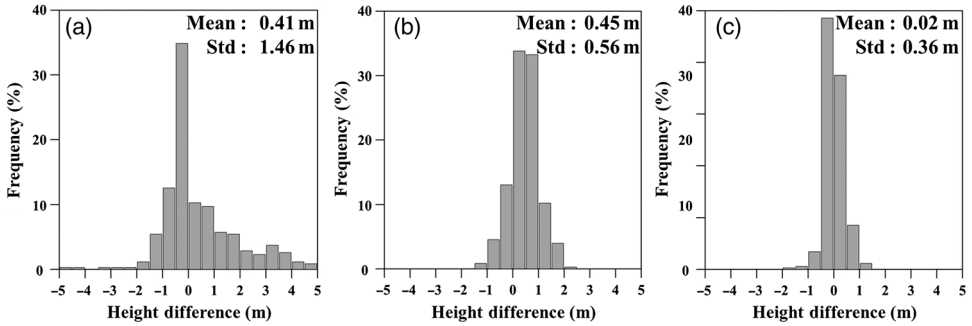

Fig. 9 Error histograms of (a) NED DEM, (b) CInSAR-derived DEM, and (c) airborne DEM. The topographic heights of the summer ICESat are used for the reference values.

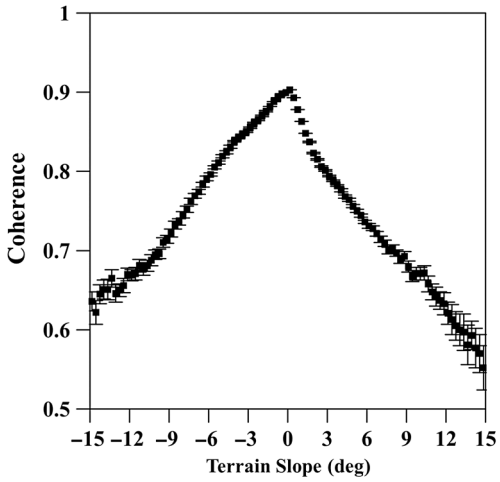

Fig. 10 Variations of coherence with respect to terrain slope.

the airborne DEM, the achieved accuracy of the CInSAR DEM is as precise as it corresponds to almost a half meter. The accuracies of CInSAR DEM and airborne DEM are slightly lower than those from the winter ICESat elevation data. This would be because the summer ICESat elevation data were acquired a few years earlier. The results have demonstrated that the CInSAR technique can create a highly accurate DEM with accuracy of submeters using cross-InSAR images from ERS and Envisat over an area of high flat land covered with ice and snow.

Figure 10 displays the variations of coherence with respect to the terrain slope obtained from the box D. The maximum of the coherence in the test area was obtained from 0 deg. The higher the terrain slope is, the lower the coherence is. The coherence of the fore slope (positive terrain slope) is lower than that of the back slope (negative terrain slope). This confirms that the coherent area of the fore slope is smaller than that of the back slope due to the foreshortening effect, as shown in Fig. 1. Figure 10 illustrates that we will not construct a valid DEM in areas including the fore and back slopes of more than 12 and 18 deg if a coherence of more than 0.6 is required to produce a highly precise DEM. This result means that the CInSAR method has a limitation in that it cannot be applied to a steep mountainous area.

4 Discussion

We have demonstrated that the CInSAR method can create DEM of submeter accuracy over high flat land covered with ice and snow. The small height ambiguity of about 4.1 m is allowed to still generate a highly precise DEM. In addition, the CInSAR method can be an efficient tool to find error patterns of the existing DEM. It is noted that we can easily identify DEM artifacts from the differential CInSAR interferogram of Fig. 5(b). As seen in Fig. 7, we cannot identify some rivers, lakes, and valleys from the errors of the NED DEM. This means that we can misunderstand the topographic features from the errors of the NED DEM. Thus, it is important that serious DEM errors are detected and corrected.

The horizontal position of the CInSAR differential interferogram is not accurate because it is matched with the horizontal position of the NED DEM of 30-m resolution. The ICESat elevation data can be used for the correction of the horizontal position. The correction could be performed precisely because a lot of ICESat elevation points were available in the study area. Moreover, the ICESat elevation data can be used for the correction of the CInSAR-derived topographic heights. This correction is allowed to effectively remove the residual orbital error in the CInSAR-derived topographic heights.

The accuracies of the CInSAR DEM estimated from the summer and winter ICESat elevation data were about 0.56 and 0.50 m, respectively. The accuracies of the airborne DEM from the summer and winter ICESat elevation data were about 0.36 and 0.34 m, respectively. If the snow depth is inconstant over the study area, the accuracy of the airborne DEM from the summer ICESat elevation must be higher than that from the winter ICESat elevation. That is because

the airborne DEM does not include the snow depth. However, the accuracies of the airborne DEM from the summer and winter ICESat elevation data are very similar. These results indicate a constant snow depth over the study area. From this test, it is very difficult to assess the radar penetration effect because the snow depth over the study area is nearly constant. However, since the C-band radar penetration is assumed to be about 1 to 2 m,[43] the accuracy of the CInSAR DEM might not be affected by the snow cover effect. We can also estimate the snow depth from the difference between the CInSAR DEM and the summer ICESat elevation data or between the airborne DEM and the winter ICESat elevation data. The estimated snow depth is about 0.45 m from the CInSAR DEM or about 0.53 m from the airborne DEM. The snow depth of about 0.53 m is more convincing because the accuracy of the airborne DEM is better and the winter ICESat data is more accurate. Thus, we can summarize that the snow depth is constantly about 0.53 m over the study area in February to March 2008.

5 Conclusions

The CInSAR is a useful method to create a precise DEM using SAR images acquired at slightly different radar carrier frequencies. The CInSAR is accomplished by using a long baseline of more than 2 km and a short repeat-time of about 29 min between a pair of successive ERS-2 and Envisat acquisitions. In this study, we have analyzed the CInSAR coherence with respect to the perpendicular baseline and the terrain slope angle. A CInSAR pair having a perpendicular baseline between 1.0 and 2.6 km is recommended if the study area consists of flat terrains of less than ± 5 deg. From a theoretical performance test, a submeter height accuracy for CInSAR-derived DEM is expected.

The optimal CInSAR procedure is used for this study and the existing NED DEM is used to generate a differential CInSAR interferogram. The NED DEM elevation discrepancies could be identified from the differential CInSAR interferogram. A DEM of ~20-m spatial resolution over an area of high flat land covered up with ice and snow in northern Alaska has been produced using the CInSAR technique and compared with the NED DEM and the airborne DEM. The CInSAR-derived DEM represents more topographic details than the NED DEM. Accuracy assessment has been carried out using the ICESat laser altimeter data of 2 cm vertical accuracy. The achieved accuracy of the CInSAR DEM is 0.50 m. This is much better than NED DEM (1.95 m) and is slightly lower than that of the airborne InSAR DEM (0.36 m). This result shows that the CInSAR technique can create a DEM with an accuracy of submeters from ERS and Envisat CInSAR pair over a high flat land. Therefore, this technique can be used for creating an accurate DEM as well as detecting the elevation changes of meter-scale even in the area where there are severe land surface changes such as the high flat land covered with ice and snow.

Acknowledgement

This research was supported by Basic Science Research Program through the National Research Foundation of Korea (NRF) funded by the Ministry of Education, Science and Technology (NRF-2012R1A1A2005801), and Zhong Lu is supported by the Shuler-Foscue Endowment at Southern Methodist University.

References

1. Z. Lu et al., "Ground surface deformation patterns, magma supply, and magma storage at Okmok volcano, Alaska, from InSAR analysis: 1. Intereruption deformation, 1997–2008," *J. Geophys. Res.* **115**, B00B02 (2010).
2. H. S. Jung et al., "Mapping three-dimensional surface deformation by combining multiple-aperture interferometry and conventional interferometry: application to the June 2007 eruption of Kilauea volcano, Hawaii," *IEEE Geosci. Remote Sens. Lett.* **8**, 34–38 (2011).
3. Z. Lu and O. Kwoun, "Radarsat-1 and ERS InSAR analysis over southeastern coastal Louisiana: implications for mapping water-level changes beneath swamp forests," *IEEE Trans. Geosci. Remote Sens.* **46**, 2167–2184 (2008).

4. L. Zhang et al., "Mapping ground surface deformation using temporarily coherent point SAR interferometry: application to Los Angeles basin," *Remote Sens. Environ.* **117**, 429–439 (2012).
5. L. Ji et al., "Episodic deformation at Changbaishan Tianchi volcano, northeast China during 2004 to 2010, observed by persistent scatterer interferometric synthetic aperture radar," *J. Appl. Remote Sens.* **7**(1), 073499 (2013).
6. J.-K. Choi et al., "Integration of a subsidence model and SAR interferometry for a coal mine subsidence hazard map in Taebaek, Korea," *Int. J. Remote Sens.* **32**, 8161–8181 (2011).
7. B. Lee and S.-K. Lee, "Delimiting boundaries of market areas of central places using the density of retail facilities in an urban space," *Int. J. Urban Sci.* **18**, 90–102 (2014).
8. W. Kuitert, "The nature of urban Seoul: potential vegetation derived from the soil map," *Int. J. Urban Sci.* **17**, 95–108 (2013).
9. A. Kumar and A. C. Pandey, "Spatio-temporal assessment of urban environmental conditions in Ranchi Township, India using remote sensing and geographical information system techniques," *Int. J. Urban Sci.* **17**, 117–141 (2013).
10. P. Raillou and M. Gelautz, "Relief reconstruction from SAR stereo pairs: the "optimal gradient" matching method," *IEEE Trans. Geosci. Remote Sens.* **37**, 2099–2107 (1999).
11. H. Arefi et al., "Iterative approach for efficient digital terrain model production from CARTOSAT-1 stereo images," *J. Appl. Remote Sens.* **5**, 053527 (2011).
12. A. Yang et al., "Three-dimensional panoramic terrain reconstruction from aerial imagery," *J. Appl. Remote Sens.* **7**, 073497 (2013).
13. H. S. Lee and N. H. Younan, "DTM extraction of LIDAR returns via adaptive processing," *IEEE Trans. Geosci. Remote Sens.* **41**, 2063–2069 (2003).
14. C.-K. Wang and Y.-H. Tseng, "Dual-directional profile filter for digital terrain model generation from airborne laser scanning data," *J. Appl. Remote Sens.* **8**, 083619 (2014).
15. G. Rufino, A. Moccia, and S. Esposito, "DEM generation by means of ERS tandem data," *IEEE Trans. Geosci. Remote Sens.* **36**, 1905–1912 (1998).
16. K. S. Rao and H. K. A. Jassar, "Assessment of shuttle radar topographic mission performance over the Kuwait desert terrain," *J. Appl. Remote Sens.* **6**, 063504 (2012).
17. B. Rabus et al., "The shuttle radar topography mission—a new class of digital elevation models acquired by spaceborne radar," *ISPRS J. Photogramm. Remote Sens.* **57**, 241–262 (2003).
18. J. H. Yu, L. Ge, and C. Rizos, "Digital elevation model generation using multibaseline advanced land observing satellite/phased array type L-band synthetic aperture radar imagery," *J. Appl. Remote Sens.* **5**, 053510 (2011).
19. H. A. Zebker et al., "Accuracy of topographic maps derived from ERS-1 interferometric radar," *IEEE Trans. Geosci. Remote Sens.* **32**, 823–836 (1995).
20. X. Zhou, N.-B. Chang, and S. Li, "Applications of SAR interferometry in Earth and environmental science research," *Sensors* **9**, 1876–1912 (2009).
21. T. Esch et al., "TanDEM-X mission—new perspectives for the inventory and monitoring of global settlement patterns," *J. Appl. Remote Sens.* **6**, 061702 (2012).
22. J. H. Gonzalez et al., "Development of the TanDEM-X calibration concept: analysis of systematic errors," *IEEE Trans. Geosci. Remote Sens.* **48**, 716–726 (2010).
23. C. Colesanti et al., "Generation of DEM with sub-metric vertical accuracy from 30' ERS-Envisat pairs," in *Proc. Fringe*, ESA, Frascatti, Italy (2003).
24. M. Santoro et al., "Observations, modeling, and applications of ERS-Envisat coherence over land surfaces," *IEEE Trans. Geosci. Remote Sens.* **45**, 2600–2611 (2007).
25. U. Wegmuller et al., "DEM generation using ERS-Envisat interferometry," *J. Appl. Geophys.* **69**, 51–58 (2009).
26. S.-H. Hong and J.-S. Won, "ERS-ENVISAT cross-interferometry for coastal DEM construction," in *Proc. Fringe*, ESA, Frascatti, Italy (2005).
27. M. Santoro, U. Wegmuller, and J. I. H. Askne, "Signatures of ERS-Envisat interferometric SAR coherence and phase of short vegetation: an analysis in the case of Maize fields," *IEEE Trans. Geosci. Remote Sens.* **48**, 1702–1713 (2010).

28. W. J. Lee, H. S. Jung, and Z. Lu, "A study of high-precision DEM generation using ERS-Envisat SAR cross-interferometry," *J. Korean Soc. Surv. Geod. Photogramm. Cartogr.* **28**(4), 431–439 (2010).
29. H. A. Fricker et al., "Assessment of ICESat performance at the salar de Uyuni, Bolivia," *Geophys. Res. Lett.* **32**, L21S06 (2005).
30. X. Li, A. Baker, and T. Hutt, "Accuracy of airborne IFSAR mapping," in *Proc. FIG*, ACSM and ASPRS, Washington, District of Columbia (2002).
31. F. Gatelli et al., "The wavenumber shift in SAR interferometry," *IEEE Trans. Geosci. Remote Sens.* **32**, 855–865 (1994).
32. D. T. Sandwell and E. J. Price, "Phase gradient approach to stacking interferograms," *J. Geophys. Res.* **103**, 30183–30204 (1998).
33. E. Rodriguez and J. M. Martin, "Theory and design of interferometric synthetic aperture radars," *IEEE Proc. Radar Signal Process.* **139**(2), 147–159 (1992).
34. H. A. Zebker and J. Villasenor, "Decorrelation in interferometric radar echoes," *IEEE Trans. Geosci. Remote Sens.* **30**, 950–959 (1992).
35. S. Remko and V. Pieter, "Precise orbit determination and gravity field improvement for the ERS satellites," *J. Geophys. Res.* **103**, 8113–8128 (1998).
36. R. Abdelfattah and J. M. Nicolas, "Topographic SAR interferometry formulation for high-precision DEM generation," *IEEE Trans. Geosci. Remote Sens.* **40**, 2415–2426 (2002).
37. J. L. Davis et al., "Ground-based measurement of gradients in the "wet" radio refractivity of air," *Radio Sci.* **28**, 1003–1018 (1993).
38. C. Werner et al., "Precision estimation of local offsets between pairs of SAR SLCs and detected SAR images," in *Proc. IGARSS*, pp. 4803–4805, IEEE, Seoul, Korea (2005).
39. D. Gesch, J. Williams, and W. Miller, "A comparison of US geological survey seamless elevation models with shuttle radar topography mission data," in *Proc. IGARSS*, pp. 754–756, IEEE, Sydney, Australia (2001).
40. B. E. Schutz et al., "Overview of the ICESat mission," *Geophys. Res. Lett.* **32**, L21S01 (2005).
41. H. J. Zwally et al., "ICESat's laser measurements of polar ice, atmosphere, ocean and land," *J. Geodyn.* **34**, 405–445 (2002).
42. R. M. Goldstein and C. L. Werner, "Radar interferogram filtering for geophysical applications," *Geophys. Res. Lett.* **25**, 4035–4038 (1998).
43. E. Rignot, K. Echelmeyer, and W. Krabill, "Penetration depth of interferometric synthetic-aperture radar signals in snow and ice," *Geophys. Res. Lett.* **28**, 3501–3504 (2001).

Won-Jin Lee is a PhD candidate at the University of Seoul, Republic of Korea. He received his BS and MS degrees in geoinformatics from the University of Seoul in 2008 and 2010, respectively. His current research interests include synthetic aperture radar (SAR), SAR interferometry, and multitemporal InSAR.

Hyung-Sup Jung received his MS and PhD degrees in geophysics and remote sensing from Yonsei University, Seoul, Republic of Korea, in 1998 and 2007, respectively. Currently, he is an associate professor with the Department of Geoinfomatics, University of Seoul, Seoul, Republic of Korea. His primary research interests include developments of SAR, InSAR, multiple-aperture InSAR (MAI) and MTInSAR processors, and 3-D deformation mapping by combining MAI and InSAR and 2-D surface velocity estimation by combining MAI and along-track interferometry.

Zhong Lu received his MS degree from Peking University, Beijing, China, in 1992 and his PhD degree from the University of Alaska Fairbanks, Fairbanks, in 1996. He is a Shuler-Foscue Chair with the Roy M. Huffington Department of Earth Sciences, Southern Methodist University, Dallas, Texas. His research interests include technique developments of SAR, InSAR, and persistent scatterer InSAR processing and their applications on natural hazard monitoring and natural resource management.